Integration methods for distributed sound sources

Merino-Martínez, Roberto; Sijtsma, Pieter; Carpio, Alejandro Rubio; Zamponi, Riccardo; Luesutthiviboon, Salil; Malgoezar, Anwar M.N.; Snellen, Mirjam; Schram, Christophe; Simons, Dick G.

DOI
10.1177/1475472X19852945

Publication date
2019

Document Version
Final published version

Published in
International Journal of Aeroacoustics

Article

aeroacoustics

International Journal of Aeroacoustics
0(0) 1–26

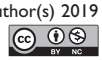

DOI: 10.1177/1475472X19852945
journals.sagepub.com/home/jae


Integration methods for distributed sound sources

Roberto Merino-Martínez[1], Pieter Sijtsma[1,2], Alejandro Rubio Carpio[1], Riccardo Zamponi[3], Salil Luesutthiviboon[1], Anwar MN Malgoezar[1], Mirjam Snellen[1], Christophe Schram[3] and Dick G Simons[1]

Abstract

Most acoustic imaging methods assume the presence of point sound sources and, hence, may fail to correctly estimate the sound emissions of distributed sound sources, such as trailing-edge noise. In this contribution, three integration techniques are suggested to overcome this issue based on models considering a single point source, a line source, and several line sources, respectively. Two simulated benchmark cases featuring distributed sound sources are employed to compare the performance of these integration techniques with respect to other well-known acoustic imaging methods. The considered integration methods provide the best performance in retrieving the source levels and require short computation times. In addition, the negative effects of the presence of unwanted noise sources, such as corner sources in wind-tunnel measurements, can be eliminated. A sensitivity analysis shows that the integration technique based on a line source is robust with respect to the choice of the integration area (shape, position, and mesh fineness). This technique is applied to a trailing-edge-noise experiment in an open-jet wind tunnel featuring a NACA 0018 airfoil. The location and far-field noise emissions of the trailing-edge line source were calculated.

Keywords

Acoustic imaging, integration methods, trailing-edge noise, porous trailing edge

Date received: 22 June 2018; accepted: 27 November 2018

[1]Section Aircraft Noise & Climate Effects (ANCE), Faculty of Aerospace Engineering, Delft University of Technology, Delft, The Netherlands
[2]Pieter Sijtsma Advanced AeroAcoustics (PSA3), Wezep, The Netherlands
[3]Environmental and applied Fluid Dynamics Department, von Karman Institute for Fluid Dynamics, Belgium

Corresponding author:
Roberto Merino-Martínez, Section Aircraft Noise & Climate Effects (ANCE), Faculty of Aerospace Engineering, Delft University of Technology, Delft, The Netherlands.
Email: r.merinomartinez@tudelft.nl

Introduction

The use of conventional acoustic beamforming techniques[1–4] incorporates the assumption of point sound sources at every scan point of a considered scan grid. In practice the noise sources are often distributed over extended regions, like along the edges of aircraft wings[5–9] or wind turbine blades.[5,10–18] For these cases, conventional beamforming fails in determining correctly the emitted sound levels, if the peak levels in the source map are considered. To overcome this issue, the source power integration (SPI) technique[11,19] was proposed, which sums and scales the results of conventional frequency domain beamforming (CFDBF) over (part of) a scan grid. The idea is to retrieve the source level of a distributed source, i.e. a single value.

A drawback of SPI is the possible contamination by noise sources outside the region of integration (ROI). For example, the region producing airfoil trailing-edge noise, e.g. measured in wind-tunnel experiments, can be heavily contaminated by "corner sources appearing at the junctions of the airfoil and the wind-tunnel walls or end plates.

For better results in the situations given above, extensions of the SPI method[20] can be considered:

- By the assumption of the presence of a line source instead of a monopole source (SPIL). SPIL was previously applied to synthetic data of trailing-edge noise in a closed-section wind-tunnel measurement heavily contaminated by background noise, in the framework of the phased-array methods menchmark[21–24] (the reader is referred to the *Description of the test cases* section for a detailed explanation). The objective was the calculation of the spectrum emitted by the line source. The SPIL method provided the best results for this case,[25] compared to other well-known methods, such as CLEAN-SC,[26–28] DAMAS,[29] functional beamforming,[30–33] covariance matrix fitting (CMF),[34] or orthogonal beamforming.[35–37]
- By the generalization of the SPIL technique to distributed sound sources on multiple ROIs. This method is called Inverse SPI (ISPI) and is introduced in this paper. ISPI is applied to realistic wind-tunnel simulations of trailing-edge noise contaminated by corner sources.

In order to assess the dependence of SPIL on its settings, a sensitivity analysis is performed. With the findings of the sensitivity analysis, SPIL is applied to an illustrative trailing-edge-noise experiment of a NACA 0018 airfoil in an open-jet wind tunnel. The purpose of this experiment was to analyze the performance of porous trailing edges[18,38–41] as a noise-reduction measure. This experiment was used since the location of the line source causing trailing-edge noise is expected to vary when porous inserts are used[42] and this parameter can be estimated using the SPIL method.

This paper is structured as follows: The *Theory* section briefly explains the basics of the SPI, SPIL and ISPI techniques. The simulated and experimental setups employed for the evaluation of these methods are introduced in the *Description of the test cases* section. The *Simulated results* section presents the comparison between the results obtained by the aforementioned integration methods, as well as other well-known acoustic imaging methods when using synthetic data. The *Sensitivity analysis for SPIL* section contains a detailed sensitivity analysis of the SPIL technique with respect to some practical parameters, such as the size and shape of the ROI. Finally, the *Experimental results* section gathers the main outcomes from the experimental campaign.

Theory

For well-separated monopole sources, CFDBF provides the correct source sound pressure levels L_p as the peak levels in the source map.[43] In practice, this situation rarely occurs. Main lobes of closely-spaced sound sources can overlap, sidelobes can deteriorate the source map, and the sound sources can be spatially distributed, such as for trailing-edge noise. In these cases, the peak levels obtained from CFDBF correspond to erroneous source levels. In addition, if coherence loss[44] applies, the main lobe becomes broader and gets reduced in strength.[43]

Different integration methods have been proposed[20] to overcome all these issues. Three of them are described below, in increasing order of sophistication.

Source power integration

In order to limit the effect of the array's point spread function (PSF), the SPI technique[11,19] was proposed. The idea of the SPI method is to *integrate* the source power within a predefined ROI, and suppose that the integrated source power is represented by a simulated unit monopole. The integrated source power needs to be scaled by determining a certain scaling factor to normalize the total source power to a unit monopole source. This scaling factor therefore represents the total sound power within the ROI.

Figure 1(a) shows an arbitrarily distributed sound source obtained from an experiment. At the jth grid point, the source power estimate is $A_{j,\mathrm{exp}}$ (with $j \in J$). By applying the SPI method, the source powers from J grid points within a predefined ROI (framed by the dashed lines) are integrated and represented by a simulated monopole source indicated by the kth grid point, as shown in Figure 1(b). The location of the simulated monopole is usually defined in the center of the ROI. Instead of $A_{j,\mathrm{exp}}$ in Figure 1(a), $A_{j,\mathrm{sim}}$ in Figure 1(b) provides the source power of the simulated monopole's PSF at the jth grid point in the ROI. Normally, the maximum value of $A_{j,\mathrm{sim}}$, i.e. the peak of the simulated monopole's PSF at the kth grid point, is considered as one. Thus, the integrated source power from the experiment needs to be scaled to match with the integrated source power of the monopole within the ROI by dividing it by the sound power P_{exp} as

$$\frac{\sum_{j=1}^{J} A_{j,\mathrm{exp}}}{P_{\mathrm{exp}}} = \frac{\sum_{j=1}^{J} A_{j,\mathrm{sim}}}{P_{\mathrm{sim}}} \tag{1}$$

where P_{sim} is typically taken as one. In order to correctly scale the integrated source power from the experiment, the sound power P_{exp} should represent the total sound power within the ROI. The value of P_{exp} can be solved from equation (1) as

$$P_{\mathrm{exp}} = \frac{P_{\mathrm{sim}} \sum_{j=1}^{J} A_{j,\mathrm{exp}}}{\sum_{j=1}^{J} A_{j,\mathrm{sim}}} = \frac{P_{\mathrm{sim}} \sum_{j=1}^{J} \left(\boldsymbol{w}_j^* \boldsymbol{C} \boldsymbol{w}_j \right)}{\sum_{j=1}^{J} \left[\boldsymbol{w}_j^* (\boldsymbol{g}_k \boldsymbol{g}_k^*) \boldsymbol{w}_j \right]} \tag{2}$$

where $\boldsymbol{C}$ is the cross-spectral matrix (CSM), $\boldsymbol{g}_k$ is the steering vector to the kth grid point, and $\boldsymbol{w}_j = \boldsymbol{g}_j / \left|\left|\boldsymbol{g}_j\right|\right|^2$ is the weighted steering vector.[11]

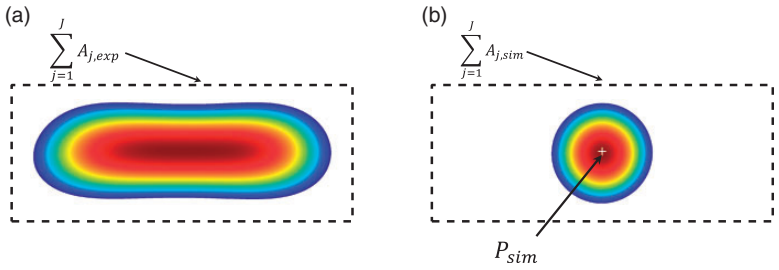

Figure 1. (a) Example of the application of the SPI technique: experimental distributed sound source and (b) simulated point source. The dashed black rectangle denotes the ROI, and the white + marker the location of the simulated point source.

For experimental measurements, the main diagonal of the CSM is usually removed to reduce the influence of noise which is incoherent for all the array microphones.[2,26] This process can give a negative source power for some grid points, which is not physically possible. Therefore, the values where $A_{j,\mathrm{exp}} < 0$ are omitted from the integration. Furthermore, the source power resulting from the sidelobes should also be excluded by setting a lower bound for inclusion of $A_{j,\mathrm{exp}}$ in the integration. Normally, a certain threshold with respect to the peak level in the source map is used.

The ROI should encompass the complete sound source (see Figure 1(a)) and be large enough to capture the potential main-lobe broadening due to coherence loss.[43] However, it should be ensured that the variation of the main lobe width is always captured in the ROI for all considered frequencies. Furthermore, the choice of the ROI should also avoid the contributions and sidelobes from other sound sources and the noise floor from the source map.[43]

This integration technique has been successfully applied to several wind-tunnel experiments[5,10–15,25] and aircraft flyover measurements,[9,45,46] yielding accurate sound pressure levels, even in the cases when coherence loss is present.[43] A similar integration technique can be applied to the results obtained with functional beamforming.[46,47]

Extension to line sources (SPIL)

In aeroacoustic measurements of leading- and/or trailing-edge noise, the presence of a line source can be expected. When a certain source distribution is known beforehand, the simulated monopole source in the SPI method can be replaced by another predefined source distribution to better represent the physical characteristics of the source. In this case, the simulated monopole is replaced by a set of linearly-arranged incoherent monopoles.

In practice, a large number of K simulated incoherent point sources of equal power level are placed along the expected location of the experimental line source with steering vectors $\boldsymbol{g}_k$, $k \in 1, 2, \ldots, K$. To obtain the line source, a minimization problem can be solved for the difference between the measured CSM ($\boldsymbol{C}$) and the CSM corresponding to the line source, $\boldsymbol{L}$. This can be formulated as

$$\min \|\boldsymbol{C} - P_{\mathrm{exp}}\boldsymbol{L}\|^2 \tag{3}$$

where $\boldsymbol{L}$ is the CSM due to the simulated line source. By solving equation (3) for P_{exp} using a least-squares approach, equation (2) is updated as

$$P_{\text{exp}} = \frac{P_{\text{sim}} \sum_{j=1}^{J} \left(\boldsymbol{g}_j^* \boldsymbol{C} \boldsymbol{g}_j \right)}{\sum_{j=1}^{J} \left[\boldsymbol{g}_j^* \left(\sum_{k=1}^{K} \boldsymbol{g}_k \boldsymbol{g}_k^* \right) \boldsymbol{g}_j \right]} = \frac{P_{\text{sim}} \sum_{j=1}^{J} \left(\boldsymbol{g}_j^* \boldsymbol{C} \boldsymbol{g}_j \right)}{\sum_{j=1}^{J} \left(\boldsymbol{g}_j^* \boldsymbol{L} \boldsymbol{g}_j \right)} \tag{4}$$

where P_{sim} now is due to *all* K simulated sources.

For distributed sound sources, the source coherence should be taken into account. However, the coherence length of a source is typically much smaller than the main lobe width, so the assumption of distributed incoherent monopoles is, in essence, valid.[43]

This technique has already been applied to trailing-edge noise measurements in an open-jet[14] and a closed-section wind tunnel[14,48] and a closed-section wind tunnel[16] with very satisfactory results.

Inverse SPI

The SPI method can be further extended to include multiple ROIs for which the simulated sources are allowed to differ in power. This is known as inverse SPI (ISPI). It addresses a similar minimization problem as the one presented in equation (3) considering Z different ROIs simultaneously (each of them with different sound powers $P_{\text{exp},z}$). It is therefore assumed that the CSM results from Z line sources. The minimization problem can be formulated as

$$\min \left\| \boldsymbol{C} - \sum_{z=1}^{Z} P_{\text{exp},z} \boldsymbol{L}_z \right\|^2 \tag{5}$$

where the Z ROIs can have different sizes. This problem needs to be solved under non-negative constraints of $P_{\text{exp},z} \geq 0$. A standard non-negative least squares (NNLS) solver can be used.[49]

This integration technique is especially useful for wind-tunnel measurements featuring mounting plates for the test model, which can cause extraneous noise sources on the junction between the test model and the mounting plates, also known as "corner" sources.[50] These sources can contaminate the results of the ROI of interest in experiments.[12–15,51] The aim of the ISPI technique is to exclude their influence on the actual results by defining dedicated ROIs at the expected locations of the "corner" sources.

In the limit of only a single grid point as the ROI, i.e. $Z = J$, the obtained method is similar to DAMAS.[29]

Description of the test cases

Synthetic line-source benchmark

This synthetic case is obtained from the phased-array methods benchmark.[21–24] (The acoustic data and more details of this benchmark case (B1) are currently available online in the following website: https://www-fs.tu-cottbus.de/aeroakustik/analytical/) The case consists

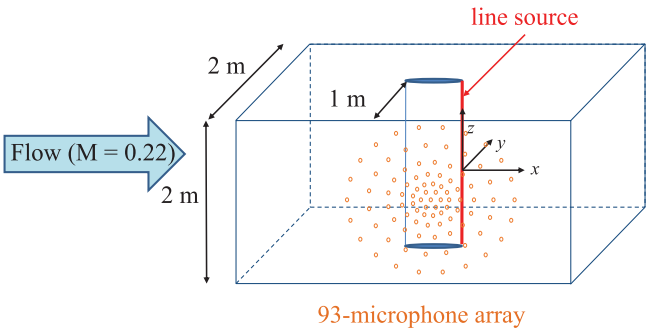

Figure 2. Diagram explaining the computational setup for the line source benchmark case. Adapted from Sarradj et al.[25]

of recorded microphone array data from a simulated acoustic line source. The measurement data were subject to severe incoherent noise. This representation is typical for measuring trailing-edge noise in a closed-section wind tunnel for which the microphones are flush-mounted in the wall of the tunnel. For recordings in this setup, noise is introduced due to the wall-boundary-layer turbulence.[25]

This benchmark case was proposed by Sijtsma (PSA3)[52] and the preliminary results obtained by several researchers using different acoustic imaging methods have been published recently by Sarradj et al.[25]

The considered coordinate system is shown in Figure 2, with the x-axis in the streamwise direction, the y-axis perpendicular to the line source and pointing away from the array plane, the z-axis in the spanwise direction of the line source pointing upwards and the center in the middle of the line source.

The setup for this case can be seen in Figure 2. A 2-m-long line source with short correlation length was simulated between $z = -1$ m and $z = 1$ m located at $x = y = 0$ m, inside of a $2\,\text{m} \times 2\,\text{m}$ cross section of a wind tunnel. Henceforth, this line source is referred to as "real" line source (see Figure 3). The line source was subject to a uniform flow with a Mach number of $M = 0.22$ in the positive x-direction. A 93-microphone array distributed in concentric circles and located at the $y = -1$ m plane with an aperture of 1.8 m was considered (see Figure 2). The presence of hard wind-tunnel walls was neglected for the simulations, i.e. no reflections are present.

A detailed explanation of the signal generation process can be found in Sarradj et al.[25] The line source was synthesized as a large number of incoherent monopoles at equal spacing and equal strengths. This results in a source strength distribution per unit length denoted as $\tilde{A}$ in Pa^2/m. The resulting source strength per frequency f for this benchmark case expressed as the sound pressure level (L_p) at the center microphone of the array, $(x, y, z) = (0, -1, 0)$ m, in dB and 50 Hz steps (resulting in a total of 200 frequencies from 50 Hz to 10 kHz) was

$$L_\text{p} = 61.16 + 0.34127f + 0.87242f^2 - 0.163f^3 + 0.0082341f^4 \tag{6}$$

where f is the frequency expressed in kHz.

On the top of the signal generated by the line source, Gaussian white noise, incoherent from microphone to microphone, was added with an L_p of 86.89 dB per frequency

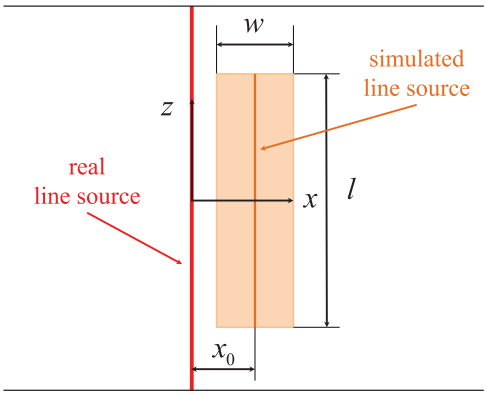

Figure 3. Diagram explaining the parameters that define the ROI (shaded in orange).

considered. This provides negative signal-to-noise ratio (SNR) values for the whole frequency range (between −25.7 dB at 50 Hz to −15.7 dB at 10 kHz), due to the varying source strength with frequency.

The challenge of this benchmark is to obtain the value of $\tilde{A}$ per frequency, expressed as the L_p at the center of the array $(x, y, z) = (0, -1, 0)$ m using the following expression[25,52]

$$L_p = 10\log_{10}\left\{\frac{\tilde{A}}{8\pi^2(1-M^2)p_{e,0}^2 h}\left[\arctan\left(\frac{l}{2h}\right)\right]\right\} \tag{7}$$

where h represents the distance between the array plane and the scan plane, l is the length of the ROI in the spanwise direction (symmetric with respect to the $z = 0$ plane) (see Figure 3), and $p_{e,0}$ is the reference effective pressure of 20 μPa. This way of expressing the results was selected in order to compare the different contributions to the benchmark. It represents the L_p observed at the center of the array if only the line source would be present.

For this case, $h = 1$ m and $l = 2$ m, so equation (7) can be simplified to

$$L_p = 10\log_{10}\left[\frac{\tilde{A}}{32\pi(1-M^2)p_{e,0}^2}\right] \tag{8}$$

Synthetic line-source and corner sources

To investigate the merits of ISPI, an additional array simulation was considered. The same microphone array was used as in the previous section. A line source was synthesized at the same position (see Figure 2), and also the same Mach number was used. The source strength distribution $\tilde{A}$ was selected such that the induced L_p (via equation (7)) in the central microphone of the array was exactly 80 dB per frequency considered. In addition, two incoherent point sources were placed at both ends of the line, representing "corner sources" due to interaction of the airfoil with the boundary layers of the wind-tunnel walls.

Figure 4. Metal foam trailing-edge insert used in the experiment. The total length of the insert is 0.06 m. Extracted from Carpio et al.[41]

These two corner sources led to an increase in L_p of more than 3 dB at the central microphone. In this simulation, no incoherent noise was added.

The challenge is to obtain the correct value of $\tilde{A}$, and thus minimizing the influence of the corner sources.

Experimental setup

The experiments were performed in the aeroacoustic vertical open-jet wind tunnel (A-Tunnel) at Delft University of Technology. It was verified that across the test section (0.4 m × 0.7 m), the freestream velocity was uniform within 0.5% and the turbulence intensity was below 0.1%. The measurements were performed on a NACA 0018 airfoil with chord $\hat{c} = 0.2$ m and span $b = 0.4$ m. The model was manufactured in aluminum using computer numerical control (CNC) machining, ensuring that the surface roughness was below 0.05 mm. The model allowed the installation of exchangeable inserts at the trailing edge with an extent of 20% of the airfoil chord (0.04 m) (see Figure 4). The insert employed in the present experiment was fabricated with "*Alantum*" NiCrAl metal foam, with cell diameter $d_c = 800$ μm and permeability $\hat{K} = 27 \times 10^{-10}$ m^2. This material was selected since it provided the highest noise reductions in the experiment performed by Carpio et al.[18] The reader is referred to Carpio et al.[40] for a detailed description of the topology and characterization of the material.

The airfoil was installed between two wooden plates of 1.2 m length, to assure the two-dimensionality of the flow,[53] and was located 0.5 m away from the outlet of the wind-tunnel nozzle (see Figure 5(a)). In order to force transition to turbulence, a tripping device consisting of carborundum elements of 0.84 mm nominal size randomly distributed over a tape of 1 cm width, placed at 20% of the chord on both suction and pressure sides and extending the whole span b (following the recommendations in Braslow et al.[54]), was used. The turbulent nature of the boundary layer was assessed using a remote wall-pressure probe. The experiments were performed at a chord-based Reynolds number of 3.95×10^5 ($V_\infty = 30$ m/s) and an angle of attack $\alpha = 0^\circ$ (which was set using a digital angle meter[41]).

The streamwise vertical coordinate system used in the present manuscript has its origin at the intersection between the trailing edge and the midspan plane of the airfoil, and the x- and z-axes are respectively aligned with the streamwise and spanwise directions, as depicted in Figure 5(a). The y-axis is perpendicular to the xz plane and points towards the microphone array.

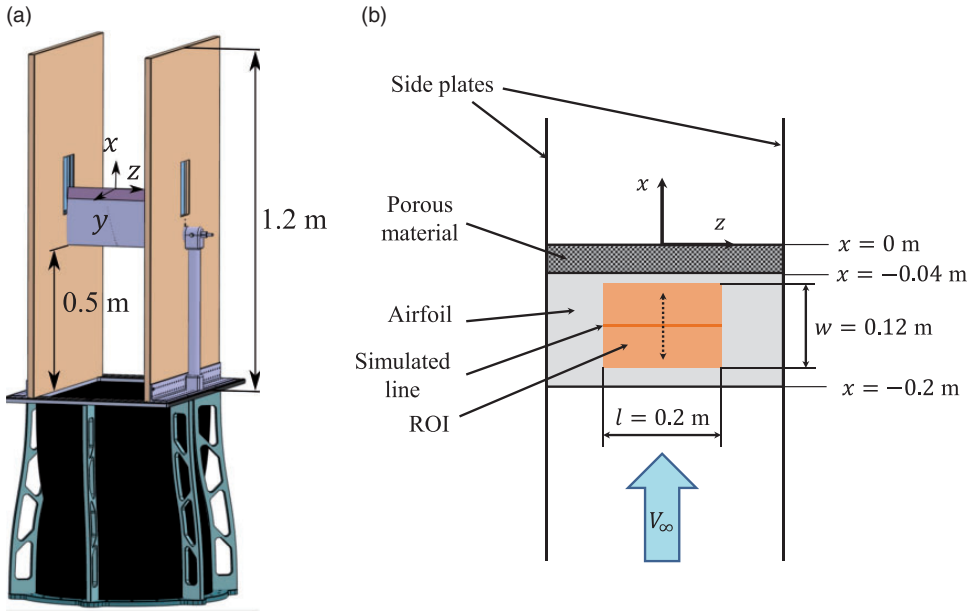

Figure 5. (a) Illustration of the experimental setup in the A-tunnel indicating the coordinate system. (b) Schematic view of the experimental setup and the location of the ROI (shaded in orange) for the trailing-edge noise measurements.

A phased microphone array consisting of 64 G.R.A.S. 40PH[55] free-field microphones with integrated CCP preamplifiers was employed for recording the far-field noise emissions of the airfoil. These microphones have a flat frequency response range of 10 Hz to 20 kHz within a sensitivity of 50 mV/Pa at 250 Hz. The microphone distribution corresponds to an adapted version of the Underbrink spiral design[2,56,57] with seven spiral arms of nine microphones each and an additional microphone located at the center of the array (see Figure 6). The diameter of the array is approximately 2 m and the distance from the array plane to the trailing edge (for an angle of attack $\alpha = 0^{\circ}$) was 1.43 m. The center microphone was approximately aligned with the center of the trailing edge of the airfoil, with coordinates $(x, y, z) = (-0.1, 1.43, 0.014)$ m.

For each measurement a sampling frequency of 50 kHz and 60 s of recording time were used. The acoustic data were averaged in time blocks of 8192 samples ($T_h = 163.84$ ms) and windowed using a Hanning weighting function with 50% data overlap, following Welch's method.[58] With these parameters, the frequency resolution is $\Delta f \approx 6.1$ Hz. The frequency range of interest for this research extended from 500 Hz to 4 kHz.

For beamforming, a scan grid covering a region ranging from $z = -0.4$ m to $z = 0.4$ m and from $x = -0.4$ m to $x = 0.4$ m was used with a spacing between grid points of $\Delta x = 0.001$ m. The results with a grid spacing of 0.01 m were also analyzed and presented negligible differences (see the *Mesh fineness* section). Figure 5 shows the position of the airfoil and the porous insert, as well as the coordinate system. The shape of the ROI is also depicted as an orange rectangle with $w = 0.12$ m and $l = 0.2$ m, placed symmetrically with respect to the x-axis and located at a random x position.

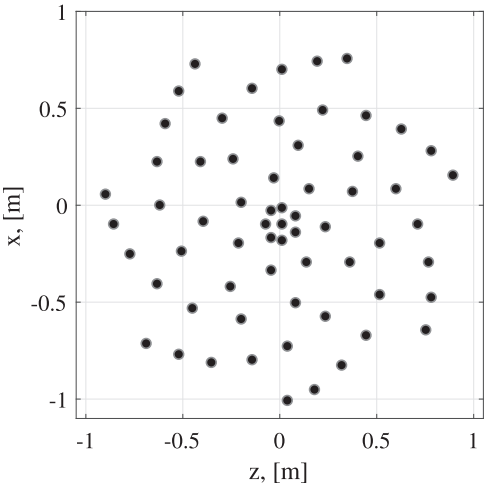

Figure 6. Microphone array distribution for the A-tunnel measurements.

Results for cases with synthetic data

Synthetic line-source benchmark

A preliminary study of the acoustic data using CFDBF confirmed that removing the main diagonal of the CSM[11] is necessary since the SNR values are very low and the influence of incoherent noise is very strong. The convection of the sound waves due to the flow inside the wind tunnel also needs to be taken into account for obtaining valid results.[11] Four source plot examples for the whole frequency range (50 Hz to 10 kHz) are presented in Figure 7 to illustrate this phenomena. The overall sound pressure levels ($L_{\mathrm{p,overall}}$) are presented. This metric accounting for K frequencies is defined as

$$L_{\mathrm{p,overall}} = 10\log_{10}\left(\sum_{k=1}^{K} 10^{L_{\mathrm{p,k}}/10}\right) \tag{9}$$

Figure 7(a) shows the beamforming results without applying the diagonal removal (DR) or convective effects; Figure 7(b) includes convective effects but no DR; Figure 7(c) includes DR but no convective effects and Figure 7(d) includes both effects. In Figure 7(a) and (b), the incoherent noise hinders any useful interpretation of the source plot and the presence of the line can barely be detected. Moreover, the $L_{\mathrm{p,overall}}$ values in these figures are considerably higher than the true ones due to the line source. After applying DR (see Figure 7(c)) the line source is clearly visible, and located at the correct position if the convective effects are accounted for (see Figure 7(d)).

Several well-known acoustic imaging methods[3] (orthogonal beamforming, CMF, functional beamforming, SPI, SPIL, DAMAS, CLEAN-SC, and Generalized Inverse Beamforming (GIBF)) were applied by different researchers using the parameters specified in Table 1. Most of the solutions obtained were extracted from Sarradj et al.[25] Only one solution per method is considered, but significant differences were found when different

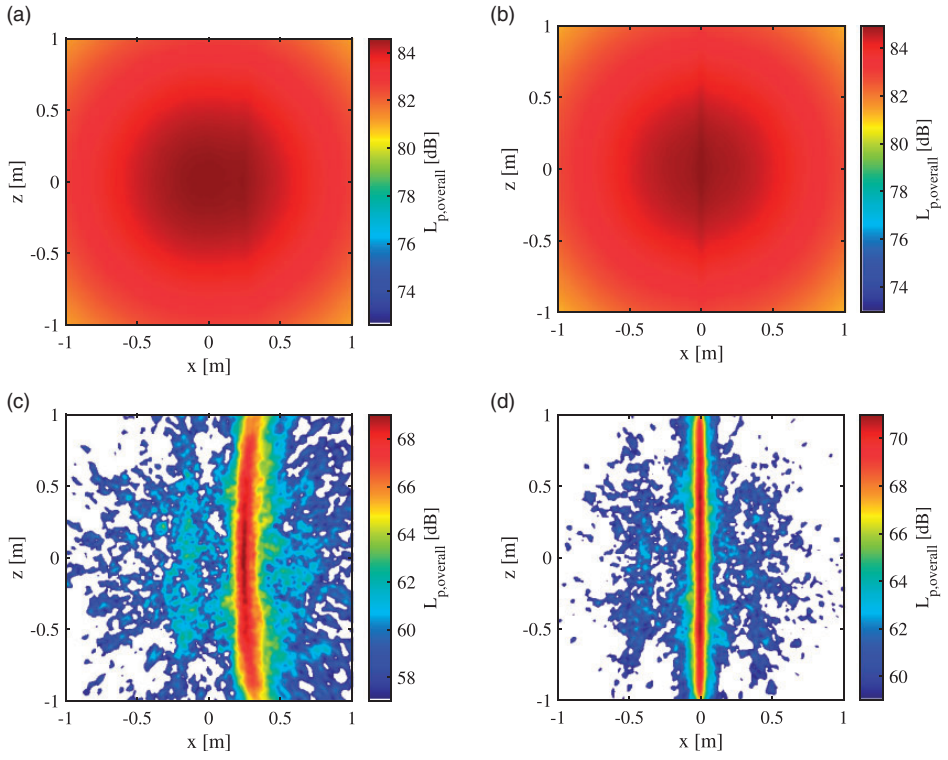

Figure 7. Obtained source maps with CFDBF for the whole frequency range (50 Hz to 10 kHz): (a) without DR or considering convective effects; (b) without DR of the CSM, but considering convective effects; (c) DR without considering convective effects; (d) DR and considering convective effects.

Table 1. Overview of the contributors and parameters for each method. Adapted from Sarradj et al.[25]

Method	Contributor	Parameters	ROI	Δx
Orthogonal	BTU	DR, $k = 16$	0.2×2 m	0.025 m
CMF	BTU	DR, NNLS solver	0.2×2 m	0.025 m
SPI	PSA3 and UniA	DR	0.08×2 m	0.02 m
SPIL	TU Delft	DR	0.08×2 m	0.02 m
SPIL	TU Delft	DR	0.04×2 m	0.01 m
Functional	TU Delft	no DR, $\nu = 50$	0.1×2 m	0.01 m
DAMAS	NASA	DR, $N_{\text{iter}} = 200$	0.12×2 m	0.02 m
CLEAN-SC	UniA	DR, $\tilde{\varphi} = 0.99$	0.08×2 m	0.02 m
GIBF	VKI	DR, L_1 norm	0.04×2 m	0.02 m

CMF: covariance matrix fitting; SPI: source power integration.

contributors applied the same method, such as DAMAS or CLEAN-SC,[25] which is not a desired feature.

In the second column of Table 1, BTU corresponds to the Brandenburg University of Technology Cottbus-Senftenberg and TU Berlin in Germany, NASA to the NASA Langley

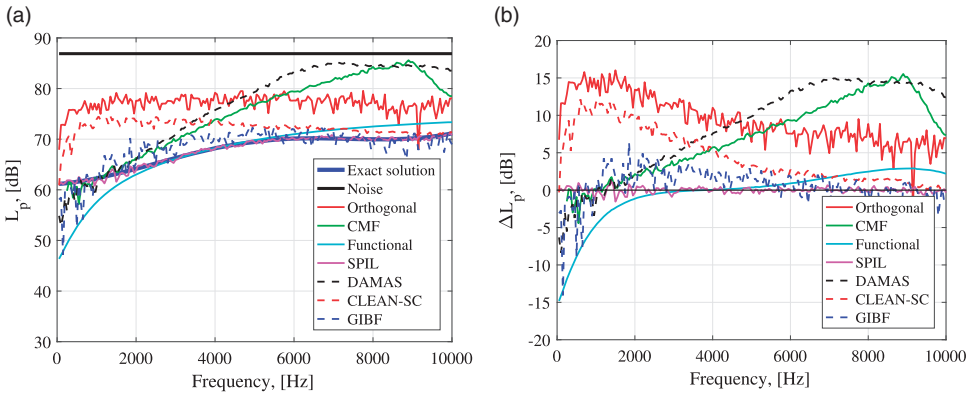

Figure 8. (a) Results of the line-source benchmark for different acoustic imaging methods. Adapted from Sarradj et al.[25] (b) Relative errors ΔL_p with respect to the exact solution for each method.

Research Center in the United States, PSA3 to Pieter Sijstma Advanced AeroAcoustics in the Netherlands, TU Delft to Delft University of Technology in the Netherlands, and UniA to the University of Adelaide in Australia.[25] In the third column of Table 1, the relevant parameters of each method are specified: k is the number of eigenvalues considered for orthogonal beamforming, ν is the functional beamforming exponent, N_{iter} is the number of iterations for DAMAS, $\tilde{\varphi}$ is the damping factor (or loop gain) for CLEAN-SC and L_1 norm is the type of regularization chosen for GIBF. The ROI employed by each contributor is stated in the fourth column of Table 1 in terms of width (w) × length (l) (see Figure 3). The spacing between grid points Δx is included in the last column. All the contributors used ROIs centered at $x = 0$ and from $y = -1$ m to $y = 1$ m, i.e. the whole span.

The frequency spectra obtained by these methods for the line-source benchmark are presented in Figure 8(a), as well as the exact solution given by equation (6). The relative errors made by each method with respect to the exact solution, $\Delta L_p = L_p - L_{p,\text{exact}}$, are included in Figure 8(b). This way, a positive value of ΔL_p means that the method overpredicts the solution. Moreover, the absolute errors made by each method averaged over the whole frequency range (i.e. over the 200 frequencies) $\varepsilon = |\Delta \bar{L}_p|$ are indicated in Table 2. In general, most methods tend to overpredict the spectrum (with the exception of functional beamforming below 2000 Hz). Orthogonal beamforming seems to considerably overpredict the results, especially at low frequencies, with errors up to about 15 dB. CMF and DAMAS present a similar behavior, but with increasing errors (up to 15 dB) for high frequencies. CLEAN-SC shows a similar trend as orthogonal beamforming but with errors about 5 dB lower. GIBF presents a comparable trend as CLEAN-SC but even closer to the exact solution, especially for lower frequencies, and it shows a good overall performance with average errors of about 1.7 dB. Surprisingly, in spite of underpredicting the results below 2 kHz, functional beamforming provides values that are in agreement with the exact solution, even though DR was not applied.[25] Optimizing the diagonal of the CSM,[59,60] instead of removing it, is of interest for future research. SPIL (with a ROI width of $w = 0.04$ m) provides the best results for this case in the whole spectrum, with an average error lower than 0.3 dB and maximum errors of 1.2 dB. In addition, the computation time required by the SPIL method is considerably lower (in the order of seconds) than other methods, especially DAMAS.

Table 2. Average absolute errors made by each method with respect to the exact solution.

Method	ε (dB)
Orthogonal ($k = 16$)	9.4034
CMF	7.2963
SPI PSA3 ($w = 0.08$ m)	0.6314
SPI UniA ($w = 0.08$ m)	0.7414
SPIL ($w = 0.08$ m)	0.3281
SPIL ($w = 0.04$ m)	0.2881
Functional ($\nu = 50$)	2.1741
DAMAS ($N_{iter} = 200$)	9.0901
CLEAN-SC	4.5769
GIBF	1.6624

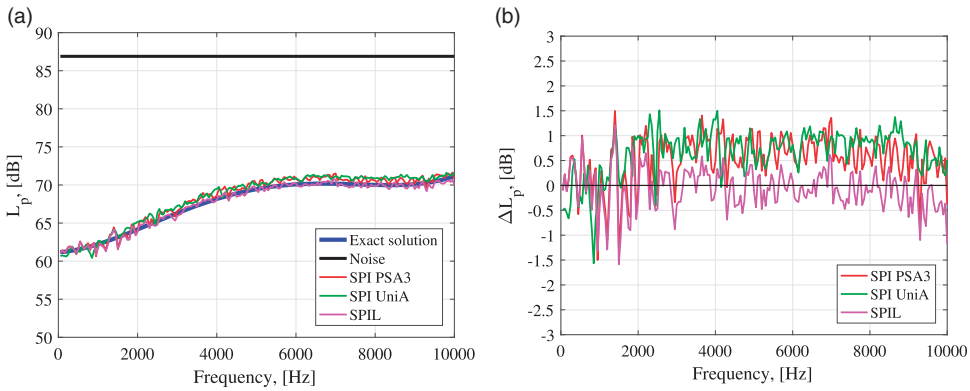

Figure 9. (a) Results of the line-source benchmark for the SPI and SPIL methods with $w = 0.08$ m. (b) Relative errors ΔL_p with respect to the exact solution for each method.

For clarity reasons, the solutions obtained by UniA and PSA3 using the SPI method were not included in Figure 8 but instead, a separate study is presented in Figure 9 comparing the performance of SPI and SPIL. In order to have a fair comparison all the ROI parameters were kept constant: $w = 0.08$ m, $l = 2$ m, $x_0 = 0$, and $\Delta x = 0.02$ m. Figure 9(a) presents the absolute spectra of both SPI and the SPIL contributions. It can be observed that the results collapse almost perfectly with the exact solution. In addition, there seems to be almost no difference between the results by TU Delft, PSA3, and UniA, suggesting that this method is more robust than other more complex methods.[25] The relative errors made by each method are depicted in Figure 9(b), with a considerably smaller scale in the y-axis than in Figure 8(b). The three contributions provide similar results, with maximum errors for single frequencies of ± 1.5 dB. However, the average absolute error made by the SPI method ($\varepsilon \approx 0.65$ dB) is approximately double than the one made by the SPIL technique ($\varepsilon \approx 0.33$ dB) (see Table 2). Therefore, the use of the SPIL method is recommended for this type of experiments, since it approximates the physics of the sound source in a better way.

The ISPI technique was not used in this benchmark case because all the incoherent monopoles had the same strength, and in this situation the ISPI technique is essentially the same as the SPIL method. A separate benchmark case to test the ISPI method is presented below.

Synthetic line-source and corner sources

Typical CFDBF acoustic images of the line source simulation with corner sources are shown in Figure 10 for different one-third-octave frequency bands. CFDBF was performed after removing the main diagonal of the CSM and correcting for the convection effects. These images show that, at low frequencies, the line source tends to be completely masked by the corner sources.

An often-used workaround for dealing with corner sources is to perform SPI on a reduced integration area in the middle of the span, away from the corners.[51] Due to the fact that L_p explicitly depends on the length of the ROI l (see equation (7)), a correction factor needs to be applied to the obtained solutions. If the whole length of the "real" line source is selected for normalizing the results (i.e. $l = 2$ m), the L_p

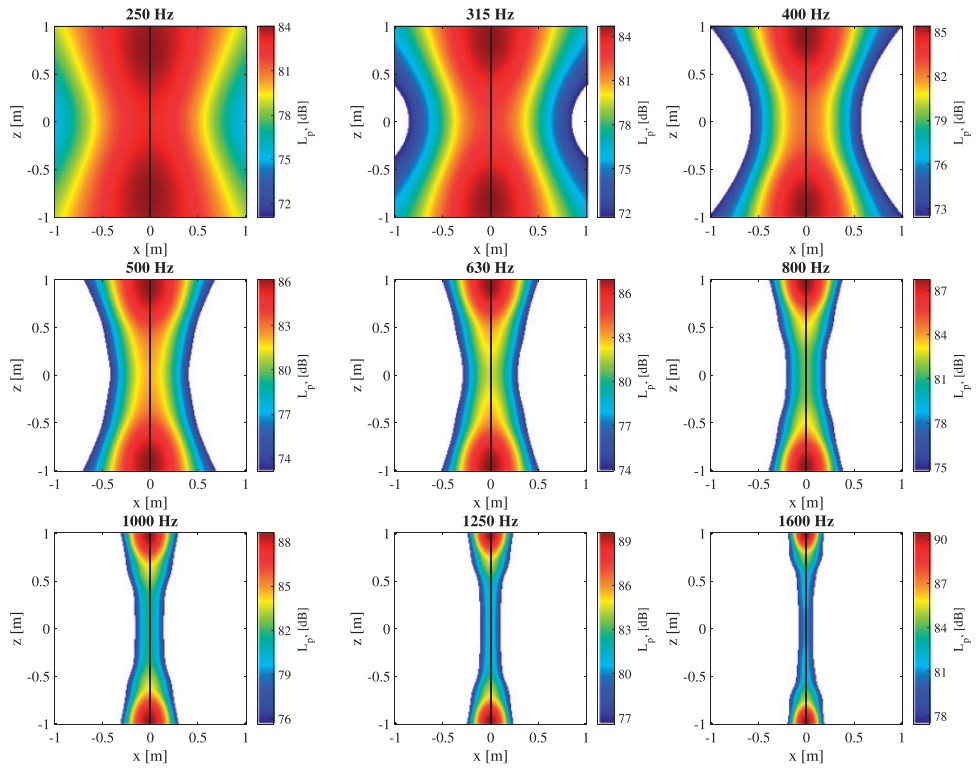

Figure 10. Source maps of the line source with corner sources obtained with CFDBF with DR for different one-third-octave frequency bands, with the respective center frequencies stated above each plot. The location of the line source is plotted as a solid black line.

obtained with the reduced integration area of length l ($L_{p,l}$) can be corrected for full span conditions by

$$L_p = L_{p,l} + 10\log_{10}\left[\frac{\frac{\pi}{4}}{\arctan\left(\frac{l}{2}\right)}\right] \tag{10}$$

where l is the length of the reduced integration area and the term $\pi/4$ comes from the solution of the arctangent term in equation (7) for the full span ($l = 2$ m and $h = 1$ m), and consequently, $\arctan(1) = \pi/4$. For low frequencies (around the Rayleigh resolution limit[61] for the two corner sources), however, this workaround is expected to fail because the influence of the corner sources becomes more important as their main lobes increase in size.

To demonstrate the added value of the ISPI method, 5 ROIs were defined (see Figure 11(a)). The span was divided into three segments. Furthermore, two ROIs were defined around the corner source locations. The width of the ROIs for all cases was $w = 0.04$ m and the mesh size was $\Delta x = 0.01$ m. The dimensions of each ROI are:

- A central ROI that goes from $z = -0.333$ m to $z = 0.333$ m, i.e. $l = 0.666$ m, shown in blue in Figure 11(a).
- Two lateral ROIs that go from $z = -0.990$ m to $z = -0.333$ m, and from $z = 0.333$ m to $z = 0.990$ m, i.e. $l = 0.657$ m for both ROIs, shown in red in Figure 11(a).
- Two corner ROIs at $z = -1$ m and $z = 1$ m, respectively.

Figure 11 shows the ISPI and the SPI results of the mid-span integration area. Results obtained with CLEAN-SC are included as well. All results were corrected for full span conditions, using equation (10). It is observed that both SPI and CLEAN-SC fail at low frequencies, say below 700 Hz. The ISPI results, however, show very small errors (with maximum differences per frequency of 0.18 dB) for the full frequency range.

The average absolute errors ε made by each method are gathered in Table 3. The three methods show relatively small errors, although for frequencies lower than 700 Hz,

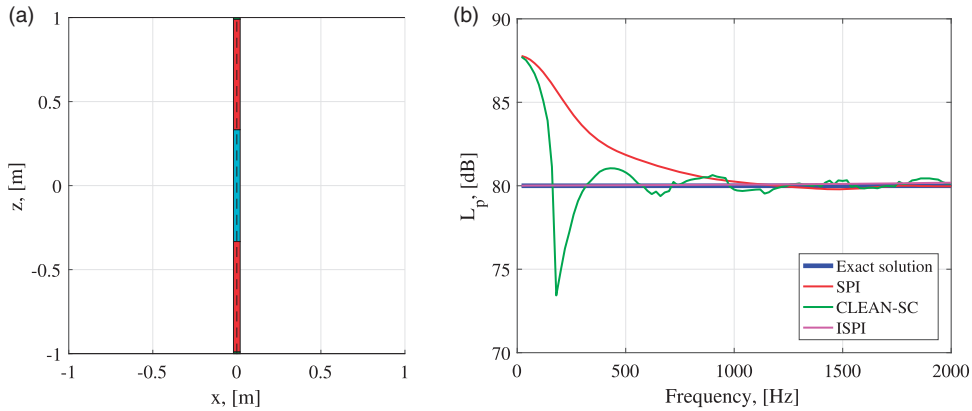

Figure 11. (a) Different ROIs considered for the ISPI method; (b) results of the line-source with corner sources benchmark for the SPI, CLEAN-SC, and ISPI methods with $w = 0.04$ m.

Table 3. Average absolute errors made by each method with respect to the exact solution.

Method	ε (dB)
SPI	1.4031
CLEAN-SC	0.9266
ISPI	0.0754

SPI considerably overpredicts the results and CLEAN-SC shows an oscillating behavior. The results obtained with the ISPI technique collapse almost perfectly with the exact solution.

Sensitivity analysis for SPIL

A sensitivity analysis was performed for the SPIL method to investigate the influence of the parameters defining the ROI. Only the SPIL method is studied here for brevity reasons, but sensitivity analyses for the SPI and ISPI techniques are expected to provide similar results. The ROI in Figure 3 (shaded in orange) has four main parameters:

1. The width in the chordwise direction w.
2. The length in the spanwise direction l.
3. The spacing between grid points Δx.
4. The location of the simulated line source chosen by the user x_0.

For simplicity sake, only integration lines parallel to the "real" line source are considered. This assumption is easily fulfilled in practical experiments where, even though the exact locations of the noise sources are not known *a priori*, the orientation of the model (such as an airfoil) with respect to the microphone array can be accurately determined. Moreover, all the ROIs considered here are symmetric with respect to the $z = 0$ plane and are contained in the $y = 0$ plane, i.e. the correct source distance to the array. The influence of the distance of the scan plane to the array was not investigated in this paper, but it has been previously addressed in the literature.[62]

Chordwise extension

Different ROI widths w were tested (considering $x_0 = 0$, $l = 2$ m and $\Delta x = 0.01$ m) and plotted in Figure 12(a). The average absolute errors ε made for each width case are presented in Figure 12(b). Acceptable results are obtained with widths up to 0.1 m (with $\varepsilon \approx 1$ dB). After that threshold value, the error rapidly increases due to the inclusion of sidelobes in the ROI, until what looks like an asymptotic value of about 9 dB at around $w = 2$ m, which is comparable to the errors presented in Table 2 for DAMAS and orthogonal beamforming. The improvement of the results by reducing w also seems to have an asymptotic behavior. For example, reducing $w = 0.04$ m to $w = 0.02$ m only reduces ε by less than 0.01 dB. Therefore, there seems to be an acceptable range of integration widths for which the SPIL method works well.

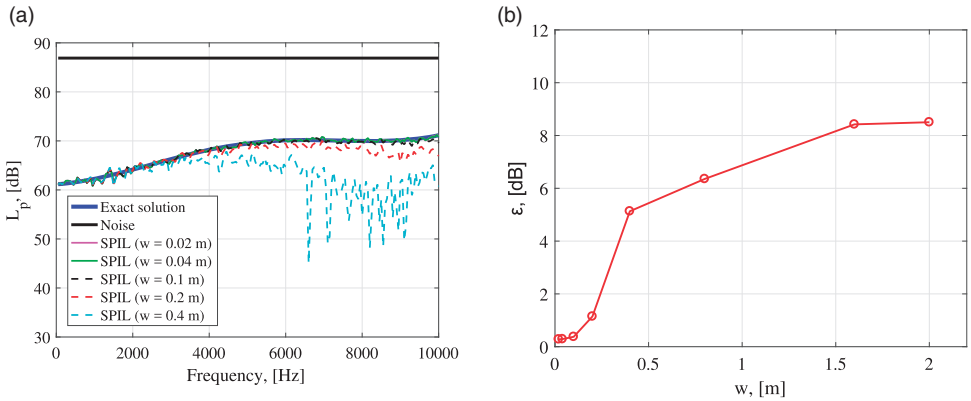

Figure 12. (a) Results of the sensitivity analysis performed for the SPIL method with respect to the ROI width *w*. Adapted from Sarradj et al.[25] (b) Average absolute errors ε made for each width case. For these results $x_0 = 0$, $l = 2$ m and $\Delta x = 0.01$ m.

Spanwise extension

As it was explained in equation (10), L_p explicitly depends on the length of the ROI l. Therefore, a correction factor needs to be applied to the solutions obtained with ROI lengths smaller than the whole span (i.e. with $l < 2$ m) (see equation (10)). This correction was not necessary for Figure 12, since the whole span was considered for every case.

To investigate the influence of the choice of the ROI length, several tests were performed using different values of l (considering $x_0 = 0$, $w = 0.1$ m and $\Delta x = 0.01$ m). The results are gathered in Figure 13(a). The average absolute errors ε made for each length case are presented in Figure 13(b). It seems that the error decreases when l is increased. The results for considerably short integration lengths still present relatively good results, with $\varepsilon \leq 2$ dB. It seems that an increasing error occurs when reducing the value of l, especially for frequencies below 2000 Hz. This is because the spanwise extension l becomes smaller than the sound wavelength at those frequencies. The influence of the spanwise extension seems to have a lower impact in the results than the chordwise extension (see Figure 12). Hence, the SPIL method is considered as robust with respect to the choice of the ROI length.

Mesh fineness

Tests were performed using several spacings between grid points Δx (considering $x_0 = 0$ m, $w = 0.04$ m, and $l = 2$ m) and plotted in Figure 14(a). The average absolute errors ε made for each width case are presented in Figure 14(b). The mesh fineness seems to hardly influence the results. Only very coarse grids ($\Delta x = 0.5$ m, i.e. only five grid points in the z direction) seem to diverge from the exact solution, especially after 9 kHz. In practice, there is normally no need for using such coarse grids. Grids with $\Delta x \leq 0.2$ m show values of ε lower than 1 dB, which is deemed as acceptable. The improvement of the results by reducing Δx seems to have an asymptotic behavior once again. For example, reducing $\Delta x = 0.01$ m to $\Delta x = 0.001$ m only reduces ε by around 0.003 dB, but increases the computation time by 100 times. Hence, the SPIL method seems to be quite robust with respect to the choice of the mesh fineness and offers acceptable results for relatively coarse grids.

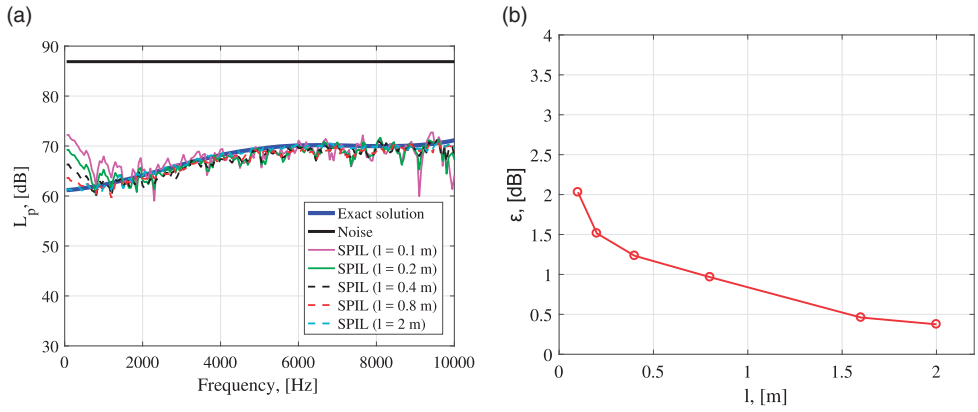

Figure 13. (a) Results of the sensitivity analysis performed for the SPIL method with respect to the ROI length l, corrected using equation (10). (b) Average absolute errors ε made for each length case. For these results $x_0 = 0$, $w = 0.1$ m and $\Delta x = 0.01$ m.

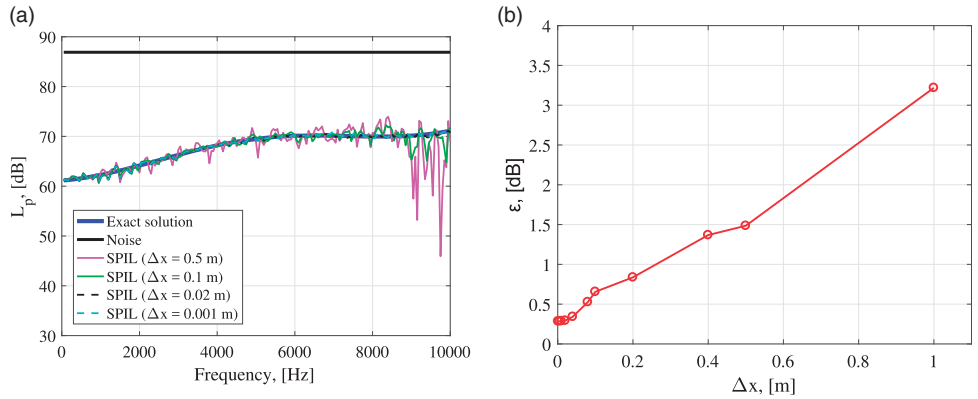

Figure 14. (a) Results of the sensitivity analysis performed for the SPIL method with respect to the spacing between grid points Δx. (b) Average absolute errors ε made for each Δx case. For these results $x_0 = 0$ m, $w = 0.04$ m and $l = 2$ m.

Line source location

One of the unknowns when measuring the trailing-edge noise in aeroacoustic experiments is the exact location of the line source. To analyze the robustness of the SPIL method with respect to this variable, several tests were performed considering different locations of the simulated line source x_0 (see Figure 3). The length of the ROI and mesh fineness were kept constant as $l = 2$ m and $\Delta x = 0.01$ m. Two different ROI widths were tested $w = 0.04$ m and $w = 0.1$ m, and the obtained frequency spectra are presented in Figure 15(a) and (b), respectively. It can be observed that the differences with the exact solution rapidly increase after a threshold value of $x_0 = 0.02$ m with errors of about 20 dB for certain frequencies. This phenomenon is even more pronounced for the narrow width case ($w = 0.04$ m).

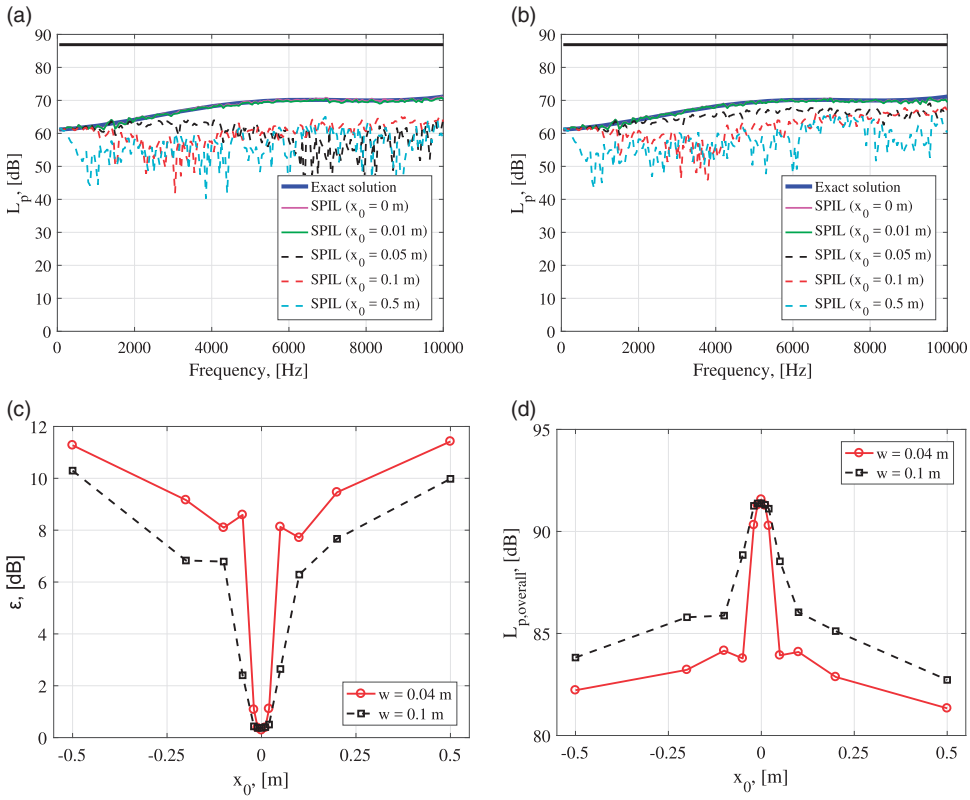

Figure 15. Results of the sensitivity analysis performed for the SPIL method with respect to the error in the line location x_0 for (a) $w = 0.04$ m and (b) $w = 0.1$ m. (c) Average absolute errors ε and (d) $L_{p,overall}$ for each x_0 case. For these results $l = 2$ m and $\Delta x = 0.01$ m.

Figure 15(c) depicts the values of ε for different values of x_0 for both cases of w. An almost-symmetric behavior with respect to $x_0 = 0$ is observed, which fits the relatively simple geometry of the benchmark. A sharp minimum of ε is found for $x_0 = 0$ for both cases, but the narrower width ($w = 0.04$ m) presents an even sharper minimum.

Figure 15(d) presents the $L_{p,overall}$ (see equation (9)) values versus x_0 for both cases of w. A similar behavior as in Figure 15(c) is observed, with the difference that, in this case, a maximum is observed for $x_0 = 0$, instead of a minimum. Once again, the narrower ROI shows a sharper peak, with still an almost-symmetric behavior with respect to $x_0 = 0$. This is an important finding in order to search for the correct location of a line source in practical cases. A fast sweep can be performed for different x_0 values using small values of w and select the x_0 value that provides a maximum for $L_{p,overall}$. In practice, the expected range of x_0 is typically in the order of centimeters, so the computational demand of this procedure is not high.

Since this parameter seems to be the most sensitive for the performance of the SPIL method, it is further investigated in the *Experimental results* section with an actual trailing-edge noise experiment. The application of porous material inserts is expected to change the location of the line source causing trailing-edge noise.[42]

A similar analysis was performed with the ISPI method with the same simulated setup as before by defining several ROIs parallel to and of the same size as those defined in Figure 11 (a) in the streamwise direction in order to estimate the location of the "real" line source. In this study, only the ROI covering the actual source positions provided the correct sound levels, whereas the rest of the ROIs only gave sound level values close to zero. This shows again the added value of the ISPI method with respect to other integration techniques.

Experimental results

Figure 16 depicts two CFDBF source plots for the trailing-edge noise measurements in the wind tunnel: one for the solid trailing edge (Figure 16(a)) and one for the porous trailing edge (Figure 16(b)). Both plots correspond to a flow velocity of $V_\infty = 30$ m/s, an angle of attack of $\alpha = 0^\circ$ and a one-third-octave band with center frequency of 1600 Hz. It can be observed that the trailing edge is indeed the dominant noise source in both cases and that the application of the porous insert in the trailing edge causes a noise reduction in the peak values of about 3 dB for this frequency band. It can be observed that the source plots in Figure 16 present lower sidelobe levels than those in Figure 7, since the SNR in the experiment was considerably higher than in the simulated line-source benchmark case.

Following the guidelines proposed in the *Sensitivity analysis for SPIL* section, Figure 17 (a) shows the $L_{\mathrm{p,overall}}$ values corresponding to the frequency range of interest (500 Hz to 4 kHz) obtained with the SPIL technique plotted with respect to the selected value of x_0 for both the solid and the porous trailing edges. The location of the maximum $L_{\mathrm{p,overall}}$ value is denoted with a red asterisk in each case. Compared with the analogous results shown in Figure 15(d), the curves in Figure 17(a) present a considerably less sharp shape, probably due to the lower frequency range considered. For illustration purposes, the beginning of the porous material insert and the trailing edge are denoted as dashed vertical black lines. It can be observed that the application of the porous material insert causes a reduction in the noise emissions of about 5 dB for the frequency range and for the range of x_0 values considered. Interestingly, the location of the maximum $L_{\mathrm{p,overall}}$ value, and hence the most likely position of the line source, also moves upwind several centimeters, approximately to the beginning of

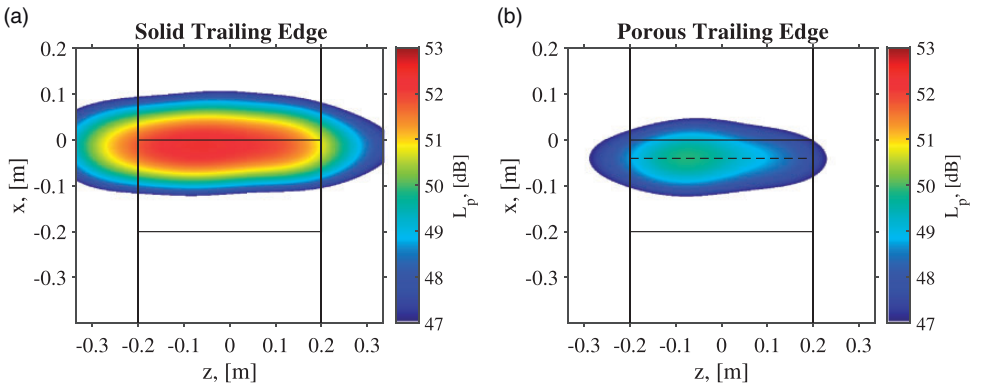

Figure 16. CFDBF source plots for a onetsesedtys.292 band with center frequency of 1600 Hz for $V_\infty = 30$ m/s and $\alpha = 0^\circ$ for (a) the solid trailing edge baseline (b) the porous trailing edge. The dashed line indicates the beginning of the porous material insert.

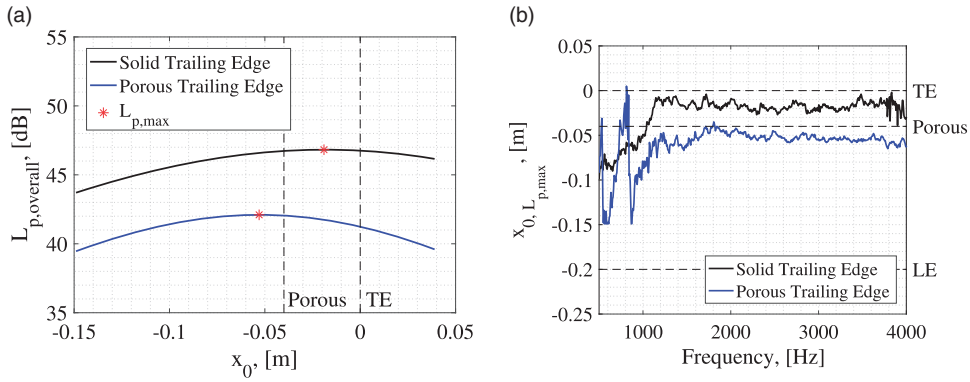

Figure 17. (a) $L_{p,overall}$ values obtained with respect to the considered location of the line source x_0 for both trailing edges. (b) Estimated locations of the line source (x_0) per frequency and for both trailing edges. The dashed black lines indicate the positions of the leading edge ($x = -0.2$ m), the beginning of the porous material ($x = -0.04$ m) and the trailing edge ($x = 0$ m).

the porous material insert ($x \approx -0.04\ \text{m} = 0.2\hat{c}$). This might be due to the acoustic impedance change caused by the presence of the porous insert instead of a solid trailing edge. In other words, the permeable–impermeable junction would act as a trailing edge, i.e. as a contributor to the noise scattered, as described by Kisil and Ayton.[42]

In order to study this phenomenon in detail, the x_0 values for which the maximum $L_{p,overall}$ is observed are plotted in Figure 17(b) with respect to the frequency for both trailing edges. The aforementioned offset in x_0 when applying the porous material insert is also observed throughout the full frequency range considered. Moreover, it can be observed that for the lower frequencies (below 1200 Hz) the estimated location of the line source in the x direction moves upwind up to about 8 cm ($\approx 0.4\hat{c}$). The porous trailing edge presents an odd increase of the x_0 values around 800 Hz. The cause for this behavior remains unknown and will be subject of future research.

With the calculated values of x_0 presented in Figure 17(b), the trailing-edge noise emissions can be estimated using equation (4) and scaled to decibels using equation (7). Figure 18 depicts the estimated noise emissions for both trailing-edge cases using the chord-based Strouhal number, $St = f\hat{c}/V_\infty$. Noise reductions due to the porous material insert are observed until a crossover Strouhal number of $St \approx 14$, which corresponds to a frequency of about 2100 Hz. After that frequency, the porous trailing edge seems to cause a noise increase. Similar behaviors were observed in previous studies in the literature.[18,38–41]

Figure 19 shows the relative noise reductions $\Delta L_p = L_{p,solid} - L_{p,porous}$ achieved by the application of the porous material insert with respect to the solid baseline. Hence, positive values of ΔL_p correspond to noise reductions. The narrow-band results with respect to the chordctons. Strouhal numbers are presented in Figure 19(a) and the ΔL_p values for each one-third-octave-band considered are depicted in Figure 19(b). Maximum noise reductions, up to approximately 10 dB, are obtained at a frequency of about 800 Hz ($St \approx 5$). After the crossover frequency of about 2100 Hz ($St \approx 14$), the porous insert causes a noise increase that becomes larger for higher frequencies, up to a 4 dB noise increase at 4 kHz ($St \approx 27$). The cause of this noise increase was suggested to be due to the additional roughness present in

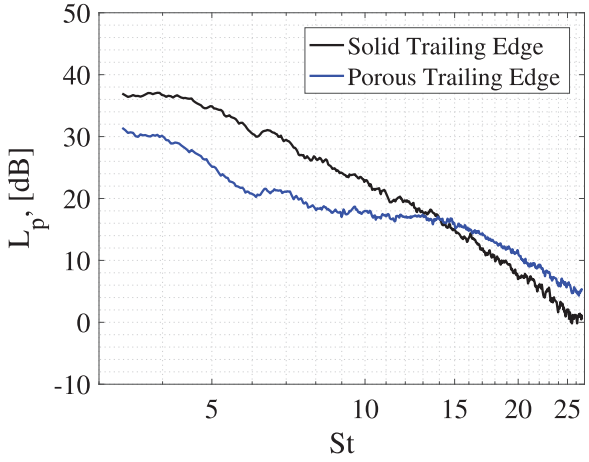

Figure 18. Integrated (using the SPIL technique) narrow-band spectra of the trailing-edge noise for both cases at $V_\infty = 30$ m/s and $\alpha = 0^\circ$. The results are presented with respect to the chord-based Strouhal number.

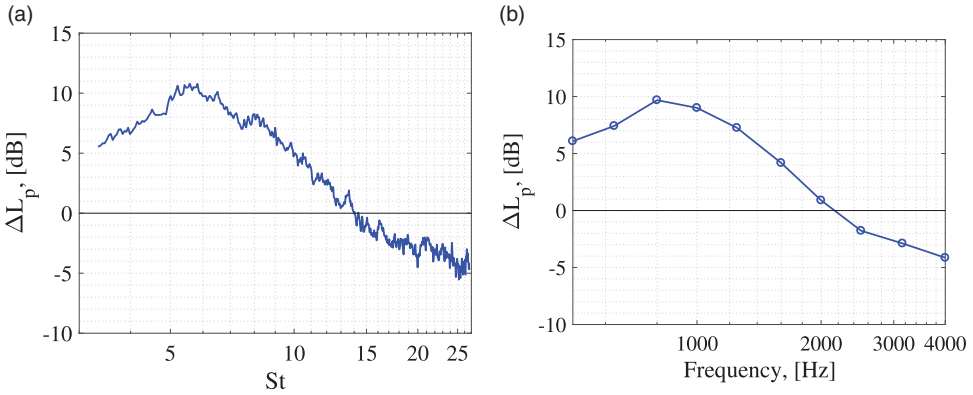

Figure 19. Relative noise reductions achieved by the porous trailing edge at $V_\infty = 30$ m/s and $\alpha = 0^\circ$. Results presented in (a) narrow-band frequencies with respect to the Strouhal number and (b) one-third-octave bands.

the porous material, which is expected to cause high-frequency noise.[38,39] This fact was confirmed for this experimental campaign by Carpio et al.[41]

Conclusions

In this paper, three integration methods intended to accurately solve distributed sound sources, such as trailing-edge noise are introduced. The first technique (SPI) is based on a single monopole source, the second one (SPIL) considers the presence of a single line source, whereas the last one (ISPI) extends the assumption to several line sources.

Explanations about how the methods work are provided and the performance of each method is evaluated in two simulated benchmark cases and compared to other well-known acoustic imaging techniques. Both benchmark cases represent examples of practical wind-tunnel measurements of trailing-edge noise. SPIL showed the best performance for the first benchmark case with respect to other methods, such as DAMAS, CLEAN-SC, or functional beamforming. ISPI outperformed SPI and CLEAN-SC, allowing for the exclusion of unwanted noise sources, such as corner sources, which are usually present in the junction between the airfoil and the wind-tunnel walls. The computational demand for the three techniques is considerably low since they are based on the CFDBF algorithm.

A sensitivity analysis for the SPIL method showed that it is considerably robust to the choice of the integration area, in both shape and position. The fineness of the grid does not seem to influence the results within a sensible range. The considered position for the simulated line source was determined to be the most sensitive parameter. Recommendations are provided for practical cases.

The SPIL method was applied to experimental measurements of the trailing-edge noise of a NACA 0018 airfoil featuring solid and porous trailing edges. The performance of porous inserts as a noise reduction measure for low-frequency noise was confirmed and a crossover frequency was observed, after which, the noise emissions increase due to the roughness of the porous material. The location of the line source seems to be displaced in the upwind direction because of the presence of the porous insert.

All in all, the use of the SPIL technique is recommended for the study of distributed sound sources with little variation in the sound level and, in case the presence of unwanted noise sources, such as corner sources, is expected, ISPI is the preferred method.

Declaration of conflicting interests

The author(s) declared no potential conflicts of interest with respect to the research, authorship, and/or publication of this article.

Funding

The author(s) received no financial support for the research, authorship, and/or publication of this article.

ORCID iD

Pieter Sijtsma https://orcid.org/0000-0001-9979-2690
Salil Luesutthiviboon https://orcid.org/0000-0002-0563-9431

References

1. Johnson DH and Dudgeon DE. *Array signal processing, concepts and techniques*. Englewood Cliffs, NJ: P T R Prentice Hall, 1993.
2. Mueller T. *Aeroacoustic measurements*. New York: Springer Science & Business Media, 2002.
3. Merino-Martinez R, Sijtsma P, Snellen M, et al. A review of acoustic imaging methods using phased microphone arrays. *CEAS Aeronaut J* 2019; 10: 197–230.
4. Merino-Martinez R. *Microphone arrays for imaging of aerospace noise sources*. PhD Thesis, Delft University of Technology, Netherlands, 2018.

5. Sijtsma P and Stoker R. Determination of absolute contributions of aircraft noise components using fly–over array measurements. In: *10th AIAA/CEAS aeroacoustics conference*, Manchester, UK, May 10–12 2004, AIAA paper 2004–2958.
6. Sijtsma P. Acoustic beamforming for the ranking of aircraft noise. Technical Report NLR-2012-137 National Aerospace Laboratory (NLR), Amsterdam, The Netherlands, 2012.
7. Snellen M, Merino-Martinez R and Simons DG. Assessment of aircraft noise sources variability using an acoustic camera. In: 5th *CEAS air & space conference. Challenges in European aerospace*, Delft, Netherlands, 7–11 September 2015, Paper 2015–019, Council of European Aerospace Societies.
8. Merino-Martinez R, Snellen M and Simons DG. Determination of aircraft noise variability using an acoustic camera. In: 23rd *international congress on sound and vibration*, Athens, Greece, 10–14 July 2016. Auburn, AL: International Inst. of Acoustics and Vibration (IIAV).
9. Snellen M, Merino-Martinez R and Simons DG. Assessment of noise level variability on landing aircraft using a phased microphone array. *J Aircraft* 2017; 54: 2173–2183.
10. Oerlemans S and Sijtsma P. Acoustic array measurements of a 1:10.6 Scaled Airbus A340 Model. In: 10th *AIAA/CEAS aeroacoustics conference*, Manchester, UK, 10–12 May 2004. AIAA paper 2004–2924.
11. Sijtsma P. Phased array beamforming applied to wind tunnel and flyneldm tests. Technical Report NNLR-TP-2010-549 National Aerospace Laboratory (NLR), Amsterdam, The Netherlands, 2010.
12. Arce León C, Merino-Martinez R, Ragni D, et al. Boundary layer characterization and acoustic measurements of flow-aligned trailing edge serrations. *Exp Fluids* 2016; 57: 1–22.
13. Arce León C, Merino-Martinez R, Ragni D, et al. Effect of trailing edge serration-flow misalignment on airfoil noise emission. *J Sound Vib* 2017; 405: 19–33.
14. Arce León C, Merino-Martinez R, Pröbsting S, et al. Acoustic emissions of semi–permeable trailing edge serrations. *Acoust Aust* 2017; 46: 111–117.
15. Arce León C, Merino-Martinez R, Ragni D, et al. Trailing edge serrations – effect of their flap angle on flow and acoustics. In: 7th *international meeting on wind turbine noise*, Rotterdam, The Netherlands, 2–5 May 2017.
16. Merino-Martinez R, van der Velden WCP, Avallone F, et al. Acoustic measurements of a DU96-W-180 airfoil with flow-misaligned serrations at a high Reynolds number in a closed-section wind tunnel. In: 7th *international meeting on wind turbine noise*, Rotterdam, The Netherlands, 2–5 May 2017.
17. Avallone F, van der Velden WCP, Merino-Martinez R, et al. Near-wall pressure fluctuations over noise reduction add-ons. In: 23rd *AIAA/CEAS aeroacoustics conference*, Denver, CO, USA, 5–9 June 2017. AIAA paper 2017–4171.
18. Rubio Carpio A, Merino-Martinez R, Avallone F, et al. Broadband trailing edge noise reduction using permeable metal foams. In: 46th *international congress and exposition of noise control engineering*, Hong Kong, 27–30 August 2017.
19. Brooks TF and Humphreys WM. Effect of directional array size on the measurement of airframe noise components. In: 5th *AIAA/CEAS aeroacoustics conference*, Bellevue, WA, USA, 1999. AIAA paper 1999–1958.
20. Merino-Martinez R, Sijtsma P and Snellen M. Inverse integration method for distributed sound sources. In: 7th *Berlin beamforming conference*, 5–6 March 2018, Berlin, Germany.
21. Bahr CJ, Brooks TF, Brusniak L, et al. Array analysis methods benchmarking – initial planning meeting. In: 20th *AIAA/CEAS aeroacoustics conference*, Atlanta, GA, USA, 16–20 June 2014.
22. Bahr CJ. Phased array methods panel session: introduction, moving forward, and discussion. In: 21st *AIAA/CEAS aeroacoustics conference*, Dallas, TX, USA, 22–26 June 2015.
23. Bahr CJ. Phased array methods panel session: introduction, year 2 progress, and discussion. In: 6th *Berlin beamforming conference*, Berlin, Germany, 29 February to 1 March 2016.

24. Bahr CJ. Phased array methods panel session: introduction, year 2 summary, and discussion. In: 22nd *AIAA/CEAS aeroacoustics conference*, Lyon, France, 30 May to 1 June 2016.
25. Sarradj E, Herold G, Sijtsma P, et al. A microphone array method benchmarking exercise using synthesized input data. In: 23rd *AIAA/CEAS aeroacoustics conference*, Denver, CO, USA, 5–9 June 2017. AIAA paper 2017–34719.
26. Sijtsma P. CLEAN based on spatial source coherence. *Int J Aeroacoust* 2007; 6: 357–374.
27. Sijtsma P, Merino-Martinez R, Malgoezar AMN, et al. High-resolution CLEAN–SC: theory and experimental validation. *Int J Aeroacoust* 2017; 16: 274–298.
28. Sijtsma P, Merino-Martinez R, Malgoezar AMN, et al. High-resolution CLEAN–SC: theory and experimental validation. In: 23rd *AIAA/CEAS aeroacoustics conference*, Denver, CO, USA, 5–9 June 2017. AIAA paper 2017–3841.
29. Brooks TF and Humphreys WM. A deconvolution approach for the mapping of acoustic sources (DAMAS) determined from phased microphone arrays. In: 10th *AIAA/CEAS aeroacoustics conference*, Manchester, UK, 10–12 May 2004.
30. Dougherty RP. Functional beamforming. In: 5th *Berlin beamforming conference*, Berlin, Germany, 19–20 February 2014.
31. Dougherty RP. Functional beamforming for aeroacoustic source distributions. In: 20th *AIAA/CEAS aeroacoustics conference*, Atlanta GA, USA, 16–20 June 2014. AIAA paper 2014–3066.
32. Merino-Martinez R, Snellen M and Simons DG. Functional beamforming applied to imaging of flyover noise on landing aircraft. *J Aircraft* 2016; 53: 1830–1843.
33. Merino-Martinez R, Snellen M and Simons DG. Functional beamforming applied to full scale landing aircraft. In: 6th *Berlin beamforming conference*, Berlin, Germany, 29 February to 1 March 2016.
34. Yardibi T, Li J, Stoica P, et al. A covariance fitting approach for correlated acoustic source mapping. *J Acoust Soc Am* 2010; 127: 2920–2931.
35. Sarradj E, Schulze C and Zeibig A. Identification of noise source mechanisms using orthogonal beamforming. In: *Noise and vibration: emerging methods*.
36. Sarradj E and Schulze C. Practical application of orthogonal beamforming. In: *Proceedings Euronoise 2006*, Tampere, Finland, 30 May to 1 June 2006.
37. Sarradj E. A fast signal subspace approach for the determination of absolute levels from phased microphone array measurements. *J Sound Vib* 2010; 329: 1553–1569.
38. Geyer T, Sarradj E and Fritzsche C. Measurement of the noise generation at the trailing edge of porous airfoils. *Exp Fluids* 2010; 48: 291–308.
39. Geyer T, Sarradj E and Fritzsche C. Porous airfoils: noise reduction and boundary layer effects. *Int J Aeroacoust* 2010; 9: 787–820.
40. Rubio Carpio A, Merino-Martinez R, Avallone F, et al. Experimental characterization of the turbulent boundary layer over a porous trailing edge for noise abatement. *J Sound Vib* 2019; 443: 537–558.
41. Rubio Carpio A, Avallone F and Ragni D. On the role of the flow permeability of metal foams on trailing edge noise reduction. In: 24th *AIAA/CEAS aeroacoustics conference*, Atlanta, GA, USA, 25–29 June 2018. AIAA paper 2018–2964.
42. Kisil A and Ayton LJ. Aerodynamic noise from rigid trailing edges with finite porous extensions. *J Fluid Mech* 2017; 836: 117–144.
43. Oerlemans S. *Detection of aeroacoustic sound sources on aircraft and wind turbines*. PhD Thesis, University of Twente, The Netherlands, 2009.
44. Ernst D, Spehr C and Berkefeld T. Decorrelation of acoustic wave propagation through the shear layer in open jet wind tunnel. In: 21*st* *AIAA/CEAS aeroacoustics conference*, Dallas, TX, USA, 22–26 June 2015. AIAA paper 2015–2976.
45. Merino-Martinez R, Bertsch L, Snellen M, et al. Analysis of landing gear noise during approach. In: 22nd *AIAA/CEAS aeroacoustics conference*, Lyon, France, 30 May to 1 June 2016. AIAA paper 2016–2769.

46. Merino-Martinez R, Neri E, Snellen M, et al. Comparing flyover noise measurements to full-scale nose landing gear wind-tunnel experiments for regional aircraft. In: 23rd *AIAA/CEAS aeroacoustics conference*, Denver, CO, USA, 5–9 June 2017. AIAA paper 2017–3006.
47. Merino-Martinez R, Neri E, Snellen M, et al. Analysis of nose landing gear noise comparing numerical computations, prediction models and flyover and wind-tunnel measurements. In: *24th AIAA/CEAS aeroacoustics conference*, Atlanta, GA, USA, 25–29 June 2018. AIAA paper 2018–3299.
48. Merino-Martinez R, Sanders MPJ, Caldas LC, et al. Comparison between analog and digital microphone phased arrays for aeroacoustic measurements. In: 24th *AIAA/CEAS aeroacoustics conference*, Atlanta, GA, USA, 25–29 June 2018. AIAA paper 2018–2809.
49. Lawson CL and Hanson RJ. *Solving least squares problems*. Englewood Cliffs, NJ: Prentice-Hall, Inc., 1974.
50. Tuinstra M and Sijtsma P. Suppression of spurioius noise sources on airfoil self-noise measurements. In: 21st *AIAA/CEAS aeroacoustics conference*, Dallas, TX, USA, 22–26 June 2015. AIAA paper 2015–2689.
51. Pagani CCJ, Souza DS and Medeiros M. Slat noise: aeroacoustic beamforming in closed-section wind tunnel with numerical comparison. *AIAA J* 2016; 54: 2100–2115.
52. Sijtsma P. Analytical benchmark 1. In: 22nd *AIAA/CEAS aeroacoustics conference*, Lyon, France, 30 May to 1 June 2016.
53. Anderson JDJ. *Fundamentals of aerodynamics*. McGraw-Hill in Aeronautical and Aerospace Engineering. 3rd ed. New York: McGraw Hill, 2001.
54. Braslow AL, Hicks RM and Harris RV Jr. Use of grit-type boundary-layer transition trips on wind-tunnel models. Technical Report NASA-TN-D-3579, NASA Technical Note (D-3579), 1966.
55. GRAS Sound & Vibration – 40PH CCP Free-field array microphone. http://www.gras.dk/products/special-microphone/array-microphones/product/178-40ph (accessed March 2017).
56. Underbrink JCS. Circularly symmetric, zero redundancy, planar array having broad frequency range applications, U.S. Patent number 6,205,224 B1. 2001.
57. Prime Z and Doolan CJ. A comparison of popular beamforming arrays. In: Society AA (ed.) *Proceedings of ACOUSTICS*, Victor Harbor, Australia, 17–20 November 2013.
58. Welch PD. The use of fast Fourier transform for the estimation of power spectra: a method based on time averaging over short, modified periodograms. *IEEE Trans Audio Electroacoust* 1967; 15: 70–73.
59. Dougherty RP. Cross spectral matrix diagonal optimization. In: 6th *Berlin beamforming conference*, Berlin, Germany, 29 February to 1 March 2016.
60. Hald J. Removal of incoherent noise from an averaged cross-spectral matrix. *J Acoust Soc Am* 2017; 142: 846–854.
61. Lord Rayleigh FRS. Investigations in optics with special reference to the spectroscope. *The London, Edinburgh and Dublin Philosophical Magazine and Journal of Science* 1879; 8(49): 261–274.
62. Sarradj E. Three-dimensional acoustic source mapping with different beamforming steering vector formulations. *Adv Acoust Vib* 2012; 2012: 1–12.